

## Structured Illumination microscopy using unknown speckle patterns. Supplementary Text and Figures

E. Mudry, K. Belkebir, J. Girard, J. Savatier, E. Le Moal, C. Nicoletti\*, M. Allain and A. Sentenac<sup>1</sup>

*Institut Fresnel (CNRS UMR 6133), \*ISM2 (CNRS UMR 6263), Université Aix-Marseille, Campus de St Jérôme, 13013 Marseille, France*

In this supplementary information, we describe the blind-SIM (for blind Structured Illumination Microscopy) algorithm that is able to estimate the sample fluorescence density from low resolution images obtained under unknown excitation patterns. We provide a numerical study of its performance with respect to noise and compare it to classical periodic SIM with known excitation patterns. Last, we apply it to simulated periodic SIM data in which the periodic excitation patterns are strongly distorted.

### 1. Blind-SIM and deconvolution algorithms

In all this work, we consider a two-dimensional imaging problem. The fluorescent sample is assumed to be infinitively thin and is placed at the object focal plane  $\Omega$  of the microscope objective. The fluorescent light is recorded at the image plane  $\Gamma$  of the microscope as in a standard epifluorescence configuration.

#### A. Statement of the problem under study

The imaging procedure can be stated as follow. An unknown density of fluorophores  $\rho$  confined in a plane  $\Omega$  is successively illuminated by  $L$  light patterns of intensity  $\{I_l\}_{l=1,\dots,L}$ . For each illumination  $l$ , the intensity  $M_l$  emitted by the fluorophores  $\rho$  is measured at plane  $\Gamma$ . The intensity  $M_l$  at a point  $\mathbf{r} \in \Gamma$  is given by the relation,

$$M_l(\mathbf{r} \in \Gamma) = \int_{\Omega} \rho(\mathbf{r}') I_l(\mathbf{r}') h(\mathbf{r} - \mathbf{r}') d\mathbf{r}', \quad (\text{S1})$$

where  $h$  denotes the detection Point Spread Function (PSF) of the microscope. Since the integral in Eq. (S1) presents a convolution structure, the numerical evaluation of the right hand side of Eq. (S1) can be performed rapidly using Fast Fourier Transforms (FFT).

#### B. Formulation of the inverse problem

The aim of the inverse problem is to determine the density of fluorophores  $\rho$  and the  $L$  illuminations  $\{I_l\}$  from the knowledge of the measured intensities  $M_l$ . Since the number of unknowns is larger than the number of data, extra information must be added. To supplement this underdetermined system, we add a constraint on the illuminations and assume that their sum is roughly homogeneous over  $\Omega$ . This condition is fulfilled in periodic SIM

where the incident light grid is translated and rotated over the sample and in speckle SIM where the speckle intensity is homogeneous in average. Under this constraint, the last illumination,  $I_L$ , can be written as a function of the  $L - 1$  other,

$$I_L = LI_0 - \sum_{l=1}^{L-1} I_l, \quad (\text{S2})$$

where  $I_0$  is a constant equal to the average intensity received by the sample. Using this constraint, we only have to evaluate  $\rho$  and the  $L - 1$  first illuminations  $\{I_l\}$ .

For sake of simplicity, Eq. (S1) is rewritten using symbolic notation as,

$$M_l = \mathbf{A}(\rho I_l), \quad (\text{S3})$$

where  $\mathbf{A}$  represents the linear operator that links the data  $M_l$  to the density of fluorophores  $\rho$  and illuminations  $I_l$ .

For a given density of fluorophores  $\rho$  and excitations  $I_l$ , one defines the residual error  $r_l$  on Eq. (S3) as follows

$$r_l = M_l - \mathbf{A}(\rho I_l) \quad (\text{S4})$$

The basic idea for solving the inverse problem is to build up two sequences related to the density of fluorophores and illuminations  $\{\rho_n\}$  and  $\{I_{l,n}\}$ , respectively, according to the following recursive relations

$$\begin{aligned} \rho_n &= \rho_{n-1} + \alpha_n d_{n;\rho}, \\ I_{l,n} &= I_{l,n-1} + \beta_{l,n} d_{l,n;I}, \end{aligned} \quad (\text{S5})$$

where  $d_{n;\rho}$  and  $d_{l,n;I}$  are updating directions with respect to the density of fluorophores  $\rho$  and illuminations  $\{I_l\}$ , respectively. The choice of these directions will be discussed later in the paper. Scalar coefficients  $\alpha_n$  and  $\beta_{l,n}$  are weights that are chosen at each iteration step such that they minimize the cost functional of the form

$$\begin{aligned} \mathcal{F}(\rho, \{I_l\}) &= \sum_{l=1}^L \|r_l\|_{\Gamma}^2 \\ &= \sum_{l=1}^{L-1} \|M_l - \mathbf{A}(\rho I_l)\|_{\Gamma}^2 \\ &\quad + \|M_L - \mathbf{A}\left[\rho \left(LI_0 - \sum_{l=1}^{L-1} I_l\right)\right]\|_{\Gamma}^2. \end{aligned} \quad (\text{S6})$$

Subscripts  $\Omega$  and  $\Gamma$  are included in the norm  $\|\cdot\|$  and later in the inner product  $\langle \cdot, \cdot \rangle$  to indicate the domain

<sup>1</sup>Correspondence should be addressed to Anne Sentenac, anne.sentenac@fresnel.fr.

of integration. The minimization of Eq. (S6) provides a maximum likelihood estimation under the assumption that the residual (S4) is an uncorrelated Gaussian noise, and, as such, does not account properly for the Poisson nature of the data. Its main advantage is that it does not require to tune any noise-related parameter. Thus, it can be used readily on any experiment. Of course, in cases where the noise has been thoroughly analysed, it may be worth deriving specially adapted algorithms [21, 22].

Substituting the expressions of  $\rho$  and  $\{I_l\}$  given in Eq. (S5) in the cost functional  $\mathcal{F}$  of Eq. (S6) leads to a polynomial of the variables  $\alpha$  and  $\beta_l$  for which the minimum is obtained thanks to a Conjugate Gradient method [23, p 413]. This ensures that  $\mathcal{F}(\rho_n, \{I_{l,n}\})$  is reduced at every step.

The updating directions  $d_{n;\rho}$  and  $d_{l,n;I}$  are based on the gradient of the cost functional  $\mathcal{F}(\rho, I_l)$ :  $g_\rho$  is the gradient of the cost functional  $\mathcal{F}(\rho, I_l)$  with respect to  $\rho$  assuming that the intensities  $I_l$  do not change within the domain  $\Omega$ ; while  $g_{l,I}$  is the gradient of  $\mathcal{F}(\rho, I_l)$  with respect to the  $l$ -th intensity,  $I_l$ , assuming that the density of fluorophores, and the  $L - 1$  other intensities do not change inside the domain  $\Omega$ . The derivation of these gradients is reported in the appendix 3 and their expressions read as:

$$g_{n,\rho} = -\sum_{l=1}^L I_{l,n-1} \mathbf{A}^\dagger r_{l,n-1}, \quad (\text{S7})$$

$$g_{l,n;I} = -\rho \mathbf{A}^\dagger (r_{l,n-1} - r_{L,n-1}). \quad (\text{S8})$$

Using gradients as updating direction being generally inefficient, one prefers to use a conjugation algorithm. We chose the Polak-Ribière conjugate gradient formula [24], known as one of the most efficient one,

$$d_{n;\rho} = g_{n;\rho} + \gamma_{n;\rho} d_{n-1;\rho} \quad \text{with} \quad \gamma_{n;\rho} = \frac{\langle g_{n;\rho} | g_{n;\rho} - g_{n-1;\rho} \rangle_\Omega}{\|g_{n-1;\rho}\|_\Omega^2}, \quad (\text{S9})$$

$$d_{n,l;I} = g_{l,n;I} + \gamma_{n;I} d_{l,n-1;I} \quad \text{with} \quad \gamma_{n;I} = \frac{\langle g_{l,n;I} | g_{l,n;I} - g_{l,n-1;I} \rangle_\Omega}{\|g_{l,n-1;I}\|_\Omega^2}. \quad (\text{S10})$$

### 1. Positivity

In many cases, the use of *a priori* information ameliorates the stability of solution with respect to noise. In our problem, the sought density of fluorophores  $\rho$  and intensities  $I_l$  are both real and positive. To incorporate this information in the reconstruction algorithm,  $\rho$  and the  $L-1$  first illuminations  $\{I_l\}$  are written as the square of auxiliary functions  $\xi$  and  $\{i_l\}$  so that,

$$\begin{aligned} I_l &= i_l^2, \\ \rho &= \xi^2. \end{aligned} \quad (\text{S11})$$

The cost functional to be minimized depends now on these auxiliary functions as,

$$\begin{aligned} \mathcal{F}(\xi, \{i_l\}) &= \sum_{l=1}^{L-1} \|M_l - \mathbf{A}(\xi^2 i_l^2)\|_\Gamma^2 \\ &+ \|\xi^2 I_L - M_L\|_\Gamma^2, \end{aligned} \quad (\text{S12})$$

with  $I_L = LI_0 - \sum_{l=1}^{L-1} i_l^2$ . As previously, one can define the derivatives of this functional with respect to  $\xi$  and  $i_l$  and perform a minimization through a gradient type algorithm. The final estimated values for  $\rho$  and  $I_l$  are then the square of the final estimates of  $\xi$  and  $i_l$ . In this case, the iterative scheme remains unchanged although the updating directions  $d_\rho$  and  $d_{l,I}$  reported in Eqs. (S5) to (S9) are rewritten with respect to  $\xi$  and  $i_l$  instead of  $\rho$  and  $I_l$ , respectively.

$$\begin{aligned} d_{n;\xi} &= g_{n;\xi} + \gamma_{n;\xi} d_{n-1;\xi} \\ \text{with} \quad \gamma_{n;\xi} &= \frac{\langle g_{n;\xi} | g_{n;\xi} - g_{n-1;\xi} \rangle_\Omega}{\|g_{n-1;\xi}\|_\Omega^2}, \\ d_{n,l;i} &= g_{l,n;i} + \gamma_{n;i} d_{l,n-1;i} \\ \text{with} \quad \gamma_{n;i} &= \frac{\langle g_{l,n;i} | g_{l,n;i} - g_{l,n-1;i} \rangle_\Omega}{\|g_{l,n-1;i}\|_\Omega^2}, \end{aligned} \quad (\text{S13})$$

where  $g_\xi$  and  $g_i$  denote the gradients of the cost functional  $\mathcal{F}$  with respect to  $\xi$  and  $i$ , respectively.

$$\begin{aligned} g_{n,\xi} &= -\sum_{l=1}^{L-1} i_{l,n-1}^2 \xi_{n-1} \mathbf{A}^\dagger r_{l,n-1} \\ &- I_{L,n-1} \xi_{n-1} \mathbf{A}^\dagger r_{L,n-1} \\ g_{l,n,i} &= -\xi_{n-1}^2 i_{l,n-1} \mathbf{A}^\dagger (r_{l,n-1} - r_{L,n-1}), \end{aligned} \quad (\text{S14})$$

### 2. Boundary effects

An important issue of the reconstruction procedure is the boundary effects. Indeed, the image on the camera of each emitting fluorophore is as large as the point spread function. Thus, fluorophores that are outside  $\Gamma$  and close to the borders may contribute to the measurements. In the same way, images of fluorophores inside  $\Gamma$  and close to the borders may be truncated. Neglecting these effects leads to strong artefacts that hinders the image interpretation. To circumvent these boundary effects, the authors apply a commonly used method in astronomy [25, 26]. The domain  $\Omega$  in which the fluorescence density and incident intensities are sought is taken larger than the image area  $\Gamma$ . More precisely, one adds on the four sides of  $\Gamma$  a large edge of width equal to twice that of the point spread function  $h$ . During the reconstruction procedure, the fluorescence density  $\rho_n$  and the incident intensities  $I_{l,n}$  can vary freely on  $\Omega$  but the measurements  $M_l$  and the residual errors  $r_{l,n}$  are only evaluated on  $\Gamma$ . Generally, the reconstructed density and illuminations over these edges are false (as there is no measurement to constrain them), but they constitute the proper boundary condition to obtain a good evaluation of  $I_l$  and  $\rho$  in the subset of  $\Omega$  that corresponds to  $\Gamma$ . All

the reconstructed density and illuminations presented in the main part of the paper are obtained with these additional edges. This technique is very efficient to remove the boundary effects except at the very borders of the image.

### 3. Initial estimates

The initial estimate of the auxiliary function corresponding to the fluorescence density,  $\xi_0$ , is taken constant equal to 1. For the periodic SIM data, the initial estimates of the  $L$  auxiliary functions corresponding to the illumination patterns  $i_{l,0}$  are homogeneous over  $\Omega$  and equal to  $\sqrt{I_0}$ . In the speckle case, better initial estimates of the illumination patterns are obtained by keeping  $\xi_0$  constant, (imposing  $d_{n,\xi} = 0$ ) during 10 iterations.

### 4. Data preprocessing

The experimental images were taken with a camera pixel size of 100 nm (when accounting for the microscope magnification) which corresponded roughly to the Nyquist criterion,  $\lambda/(4NA)$ . Before using the reconstruction procedure, the pixel was reduced by a factor of two by interpolating the measurements using zero padding in the Fourier space. Provided that the Nyquist criterion is satisfied initially, this procedure does not create artefacts [27].

The unavoidable small experimental drift was corrected by registrating the images with sub-pixel accuracy [28]. For each experiment, we estimated accurately the detection point spread function by averaging the fluorescence density of registrated isolated fluorophores. Note that we did not correct for the photobleaching effect or the intensity fluctuations since they can be included in the intensity reconstruction.

### 5. Computational effort

The dominant operation in the blind-SIM algorithm is the convolution product Eq. (S1) included in the operators  $\mathbf{A}$  and  $\mathbf{A}^\dagger$ . This operation, which has to be done several times for each illumination is made using Fast Fourier Transforms (FFT). Thus, at each iteration  $n$  the computational effort is in  $\mathcal{O}(LN \log(N))$ , where  $N$  is the number of pixels in  $\Omega$  and  $L$  is the number of illuminations. Typically, using our Fortran implementation of the algorithm on one core of an Intel Xeon processor, the computations for Fig. 3 of the main letter,  $L = 150$ ,  $N = 115600$  took 95s per iteration; and the computations for Fig. 4 of the main letter,  $L = 24$ ,  $N = 40000$  took 2.50s per iteration.

### C. Deconvolution of the wide-field images obtained under uniform illumination

It is well known that the positivity *a priori* information included in any inversion algorithm permits the recovery of sample high spatial frequencies that are not accessible with the imaging procedure (and not always present in the sample) [29]. Hence, it is necessary to check that the

resolution amelioration that we observed in the reconstructed fluorescence maps comes from the physical process of combining different structured illuminations and not only from the inversion procedure. We thus adapted our algorithm in order to estimate the fluorescence density from one single image of the same sample obtained under uniform illumination. The fluorescence density  $\xi^2$  is estimated by minimizing the functional,

$$\mathcal{F}(\xi) = \|M - \mathbf{A}(I_0 \xi^2)\|_F^2, \quad (\text{S15})$$

where  $M$  is the image obtained with the uniform illumination  $I_0$ , with a conjugate gradient technique. Our approach amounts to deconvolving the image with a positivity constraint. We then compared the reconstructed fluorescence map obtained from the single image with uniform illumination to the one obtained by processing the  $L$  speckle images. As the two experiments should exhibit the same signal to noise ratio to provide a fair comparison, the single image with uniform illumination was simply generated by summing the  $L$  images of the structured illumination experiment. The result of this study, displayed in Fig. 2 (c), 3 (f) and 4 (b) of the main letter points out clearly the role of the structured illumination in the resolution improvement.

### D. Regularization and stopping criterion

As it stands, both blind-SIM and deconvolution algorithms are not well regularized. They converge towards meaningless images in which the noise is amplified. To circumvent this often encountered issue, a Tikhonov or a Total variation regularization term is usually added to the cost functionals. The weight of the additional regularized term is optimized by forming many reconstructions of the same sample with different parameters and eventually choosing the "most appropriate" one (for instance, by the mean of the L-Curve [30], GCV [31], or even 'by eye'). To bypass this rather long procedure (that must be repeated as soon as the experimental conditions are modified), we have chosen an algorithm-dependent regularization which consists in stopping the reconstruction before convergence.

Indeed, the specificity of gradient-type algorithms is that the spatial frequency content of the reconstructions increases with the iteration number. At the beginning of the iterative process, the introduced spatial frequencies stem from meaningful information contained in the data. Then, after a certain number of iterations, they correspond essentially to the high-frequency noise. Early-stopping of the iterative process is known as a simple (but efficient) regularization technique [32] that basically acts as a Tikhonov regularization. Furthermore, because the iteration number controls the regularity of the solution, the practitioner (e.g., a biologist) can choose "by eye" the solution with the best trade-off between resolution and noise amplification. The stopping point will depend essentially on the signal to noise ratio and on the theoretically accessible spatial frequencies of the imaging

system. Practically, the appearance of noise-induced features in the reconstruction is easily seen, with increasing speckle-like background and pixellized structures.

As we are using the same gradient-type algorithm in the blind-SIM and the deconvolution methods, this algorithm-dependent regularization procedure acts in a similar way for all our data process. We stopped the iterations at the appearance of some pixellisation (for the synthetic data) or for a given level of background noise (for the experimental data). Using this criterion, the inversions were stopped at different iteration steps depending on the experiments. In Figs. 1 and 2 the blind-SIM algorithm was stopped at the 400th iteration step while the deconvolution algorithm was stopped at the 150th step. In Figs. 3 and 4 the blind-SIM algorithm was stopped at the 200th iteration step while the deconvolution was stopped at the 100th step.

## 2. Simulations and study of the resolution of blind-SIM images with respect to noise.

To study numerically the performances of blind-SIM, we considered a flat two dimensional 'star-like' sample whose fluorescence density is given by

$$\rho(r, \theta) \propto [1 + \cos(4\theta)] \quad (\text{S16})$$

where  $(r, \theta)$  are the polar coordinates of  $\mathbf{r}$  in the sample plane. This radial sample is particularly convenient for studying the performances of imaging techniques. Indeed, its radial features dwindle as one moves closer to the image center and there is always a limit radius under which they are not recovered.

The sample is placed at the object focal plane of a microscope objective of numerical aperture  $\text{NA} = 1.49$ . It is imaged with the detection point spread function,

$$h(r, \theta) = (J_1(\text{NA}k_0r)/k_0r)^2 k_0^2/\pi \quad (\text{S17})$$

where  $J_1$  is the first order Bessel function of the first kind and  $k_0 = 2\pi/\lambda$  is the free-space wavenumber with  $\lambda$  being equal to the emission and the excitation wavelengths. The images are simulated following Eq. (1) of the main letter and corrupted with Poisson noise and an additional gaussian noise corresponding to the electronic noise. The image pixel size taken in all the simulations is  $\lambda/20$ .

### A. Simulation of the data presented in Figs. 1 and 2 and in Fig. S3

In Figs. 1 and 2 of the main letter, the sample is illuminated by 160 different fully developed speckles. The latter are calculated as a sum of plane waves with random phases uniformly distributed between  $[0, 2\pi]$  and transverse wavenumbers varying from 0 to  $\text{NA}_{\text{eff}}k_0$ . The photon budget, i. e. the *total* amount of photons detected by one pixel is 20,000 on average. It corresponds to 20,000/160 photons per pixel and per image. The gaussian noise standard deviation used in this simulation corresponds to 7 photons per pixel and per measurement. It

may be more meaningful to express the noise and photon budget for pixel size corresponding to the Nyquist criterion, (i. e. with size  $\lambda/(4\text{NA}) \approx \lambda/6$ ). In this simulation, the average photon budget on the Nyquist pixel is about 200,000 yielding a photon noise of standard deviation about 0.2%. This high signal to noise ratio had been chosen to allow the investigation of the fundamental limit of the algorithm, especially when increasing the illumination patterns spatial frequencies beyond the detection band-pass. The images displayed in Fig. S3, which illustrate the performance of blind-SIM on synthetic strongly distorted periodic SIM data, are obtained in the same conditions as that of Figs. 1 and 2 (except for the illuminations which are quasi-periodic).

### B. Study of blind-SIM resolution versus noise

In this paragraph, we analyse the resolution gain achieved by blind-SIM versus the photon-budget of the experiment. We study three different excitation patterns, the standard homogeneous illumination, the speckle illumination and the periodic illumination. For the speckle configuration, 80 images are simulated with different speckle patterns generated with  $\text{NA}_{\text{eff}} = \text{NA}$ . For the periodic configuration, 9 images are simulated using a periodic light grid with period  $d \approx \lambda/(1.4\text{NA})$  which is translated by  $n(d/3)$ ,  $n = 0, 1, 2$  and rotated by  $m(2\pi/3)$ ,  $m = 0, 1, 2$ . The one-shot homogeneous illumination, the 9-shot periodic illuminations and the 80-shot speckle illuminations are simulated with the same total amount of detected photons per pixel (on average).

The reconstructed images obtained under periodic and speckle illumination using blind-SIM (Periodic blind-SIM and Speckle blind-SIM) are compared to the wide-field image (Wide-Field), its deconvolution (Deconvolution) obtained with the non-linear algorithm described in paragraph 1-C, and the reconstruction of the periodic SIM data obtained by assuming that the excitation patterns are perfectly known (Periodic SIM). In this last case, the inversion process is similar to blind-SIM except that the  $\{I_i\}$  are fixed to their actual values and the iterative search is performed only on the fluorescence density [33]. The fact that all the reconstruction procedures include the same regularization terms permits a fair comparison between the different imaging techniques and allows one to focus on the role of the (known or unknown) excitation patterns.

We consider a realistic experiment in which the total photon budget detected on average on one Nyquist pixel is about 10,000 and the electronic noise standard deviation corresponds to 6 photons per Nyquist pixel and per measurement. In this case, the photon noise is dominant and reaches 1% which is typical of most structured illumination experiments. We plot in Fig. S1 the Wide-field, Deconvolution, Speckle blind-SIM, Periodic blind SIM and periodic-SIM images together with one example of the speckle data. We observe that Periodic SIM, Speckle blind-SIM and Periodic blind-SIM allow a better reconstruction of the radial periodic pat-



tern than the Deconvolution or Wide-field. The reconstructed pattern is more contrasted in the periodic SIM image than in the periodic and speckle blind-SIM images but the limit radius under which the modulation disappears is roughly the same for the three techniques. To support this assertion quantitatively, we analysed specifically the values of the reconstructed fluorescence density along centered circles of various radius. The sample fluorescence density taken on a circle of radius  $R$  reads  $f_R(s) \propto 1 + \cos(2\pi s/L(R))$  where  $s$  is the arclength along the circle and  $L(R) = 2\pi R/40$  is the period of the pattern, which decreases as  $R$  tends to zero. To estimate the ability of the reconstruction procedures to retrieve this oscillating pattern as a function of  $R$ , we calculated the modulation contrast  $C(R) = 2\hat{f}_R(1/L(R))/\hat{f}_R(0)$  where  $\hat{f}_R$  is the one-dimensional Fourier transform of  $f_R(s)$ . For the actual sinusoidal fluorescence density of the sample,  $C(R) = [\max(f_R) - \min(f_R)]/(\max(f_R) + \min(f_R)) = 1$  whatever  $R$ .

We display in Fig. S2 the modulation contrasts obtained for the Wide-field, Deconvolution, Periodic blind-SIM, Speckle blind-SIM and periodic SIM images as a function of the period,  $L(R)$ . This plot shows that the deconvolution procedure permits to increase significantly the modulation contrast for periods bigger than the Rayleigh criterion  $L_0 = 0.6\lambda/\text{NA} \approx 0.4\lambda$  (namely it corrects the triangular low-pass detection filter), but marginally enhances the modulation contrast for periods smaller than  $L_0$ . On the other hand, speckle blind-SIM, periodic blind-SIM and periodic SIM recover the sample periodic pattern down to periods about  $L_0/2$ . To mimic the Rayleigh criterion, we defined the resolution of the reconstructed image as the period for which the contrast is about 0.10 [34], i. e. the modulation is still 'eye-visible'. With this definition, the resolution of the blind-SIM techniques is similar to that of periodic-SIM. Yet, the modulation contrast being better enhanced by periodic SIM than by blind-SIM, the periodic-SIM image remain visually more satisfactory than the blind-SIM images, see Fig. S1.

We perform the same analysis on many other simulated data with total photon budget detected on one Nyquist pixel ranging from 40,000 to 600 (on average), see Fig. S4. Except for the 600 photon-budget experiment for which the electronic noise has a one photon standard deviation (which corresponded roughly to that of an Electron Multiplying Charge Coupled Device camera), we introduce a standard electronic noise of 6 photons per pixel and per measurement for modeling the camera performance. These values encompass a wide variety of experiments from the imaging of isolated fluorophores to that of continuous samples with high fluorescence density such as those presented in the main letter. In all these examples, the modulation contrast curves with respect to  $L(R)$  obtained by the blind-SIM techniques resemble that depicted in Fig. S2. They are below the periodic-SIM curve, but remain above 0.1 for periods close to  $L_0/2$ , even with very noisy data, see Ta-

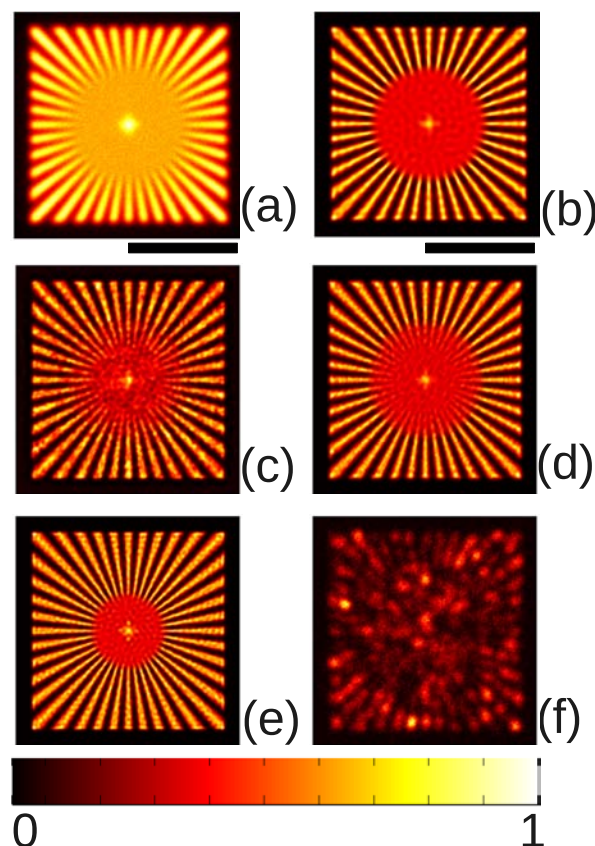


Fig. S1. **Reconstructed fluorescence density of the 'star-like' sample using various imaging techniques.** Simulated data are obtained with a total photon budget detected on average on one Nyquist pixel of 10,000 and 6 electrons read-noise per Nyquist pixel per measurement. (a) Wide-Field. (b) Deconvolution of (a). (c) Speckle blind-SIM. (d) Periodic blind-SIM. (e) Periodic-SIM (with known illumination patterns). (f) one example of the 80 measurements used for the Speckle blind-SIM reconstruction in (c). The black bars are  $5\lambda$ -long.

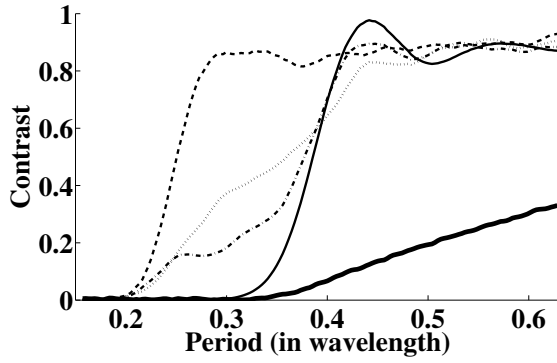


Fig. S2. Contrast of the recovered fluorescence periodic density as a function of the period extracted from the images displayed in Fig. S1. Thick solid line : Wide-Field. Thin solid line : Deconvolution. Dotted line : Speckle blind-SIM. Dash-dotted line : Periodic blind-SIM. Dashed line : Periodic SIM (with known illumination patterns).

ble S1. Actually, increasing the signal to noise ratio permits essentially to ameliorate the modulation contrast for the intermediary periods, between  $L_0$  and  $L_0/2$  as seen in Fig. S4.

This analysis demonstrates the ability of blind-SIM to recover sample high spatial frequencies beyond the detection cut-off even with noisy data and points out the interest of speckle illumination. Note that the granulo-metric aspect of the speckle blind-SIM image stems from the residual inhomogeneity of the average illumination, which is performed over 80 different speckles only, and could be reduced by taking more images. Moreover, we believe that there is still room for algorithmic improvements for enhancing the modulation contrast of the intermediary periods.

|                    | 40,000 | 10,000 | 2,500 | 600  |
|--------------------|--------|--------|-------|------|
| Wide-Field         | 0.43   | 0.43   | 0.43  | 0.43 |
| Deconvolution      | 0.33   | 0.35   | 0.36  | 0.36 |
| Speckle blind-SIM  | 0.22   | 0.23   | 0.26  | 0.32 |
| Periodic blind-SIM | 0.23   | 0.23   | 0.25  | 0.29 |
| Periodic SIM       | 0.21   | 0.22   | 0.24  | 0.29 |

Table S1. Resolution in  $\lambda$  unit of the reconstructed fluorescence density of the 'star-like' sample obtained with different imaging techniques versus the total amount of photons detected on average on one Nyquist pixel. The Rayleigh criterion is  $L_0 = 0.6\lambda/\text{NA} \approx 0.4\lambda$ . With our definition, blind-SIM resolution is comparable to classical periodic-SIM except at very low signal to noise ratio. Yet, periodic-SIM yields images which are visually more satisfying than blind-SIM, as seen in Fig. S4, because the contrast of the periodic patterns are better enhanced.

### 3. Appendix: Derivation of the gradients of the cost functional

The iterative scheme that determines the density of fluorophores and the illuminations involves gradients of the cost functional  $\mathcal{F}$  given in Eq. (S6). Let  $g_\rho$  be the gradient of  $\mathcal{F}$  with respect to  $\rho$ . It is defined as the function that maximizes the directional derivative  $D^\rho$  of  $\mathcal{F}$  with respect to  $\rho$ . The directional derivative  $D^\rho$  along a direction  $u$  reads,

$$\begin{aligned} D^\rho(u) &= \lim_{t \rightarrow 0} \frac{\mathcal{F}(\rho + tu, I) - \mathcal{F}(\rho, I)}{t} \\ &= -2 \sum_{l=1}^L \langle r_l | \mathbf{A}(I_l u) \rangle_\Gamma \\ &= -2 \sum_{l=1}^L \langle I_l \mathbf{A}^\dagger r_l | u \rangle_\Omega, \end{aligned} \quad (\text{S18})$$

where  $\mathbf{A}^\dagger$  is the adjoint operator of  $\mathbf{A}$ . The gradient  $g_\rho$ , i.e. a function  $u$  that maximizes  $D^\rho(u)$ , is given by

$$g_\rho = - \sum_{l=1}^L I_l \mathbf{A}^\dagger r_l. \quad (\text{S19})$$

Similarly to this gradient, the gradient  $g_{l,I}$  of the cost functional  $\mathcal{F}$  with respect to the intensity  $I_l$  is derived from the directional derivative  $D_l^I$  of  $\mathcal{F}$  with respect to  $I_l$ ,

$$\begin{aligned} D_l^I &= \lim_{t \rightarrow 0} \frac{\mathcal{F}(\rho, I_l + tu) - \mathcal{F}(\rho, I)}{t} \\ &= -2 \langle r_l | \mathbf{A}(\rho u) \rangle_\Gamma + 2 \langle r_L | \mathbf{A}(\rho u) \rangle_\Gamma \\ &= -2 \langle \rho \mathbf{A}^\dagger (r_l - r_L) | u \rangle_\Omega. \end{aligned} \quad (\text{S20})$$

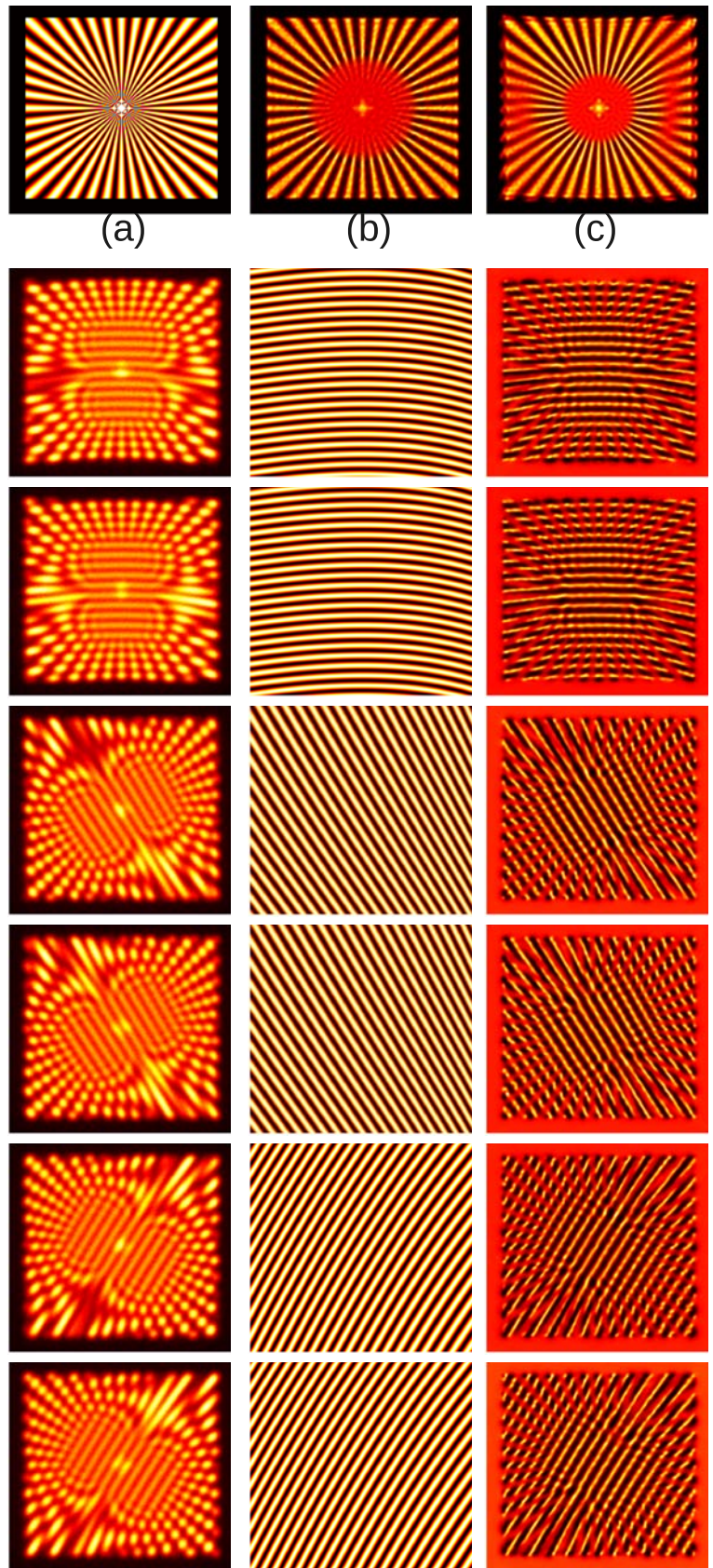
Thus,

$$g_{l,I} = -\rho \mathbf{A}^\dagger (r_l - r_L). \quad (\text{S21})$$



#### 4. Supplementary Figures

Fig. S3. **Reconstructed fluorescence density of the 'star-like' sample and reconstructed illumination patterns given by blind-SIM for a distorted periodic SIM experiment.** The sample is placed at the object focal plane of an objective with  $NA = 1.49$  and is illuminated by a periodic light grid with period  $d \approx \lambda/(1.4NA)$  which is translated by  $n(d/4)$ ,  $n = 0, 1, 2, 3$  and rotated by  $m(2\pi/3)$ ,  $m = 0, 1, 2$ . For each simulated image, the periodic illumination pattern is distorted with a different aberration. The total amount of photons detected by one Nyquist pixel is equal to 200,000 in average (0.2% noise). (a) Actual fluorophore density of the 'star-like' sample ; (b) fluorophore density reconstructed from the 12 measurements using blind-SIM. The reconstruction is free of any artefact ; (c) fluorophore density reconstructed from the 12 measurements using an algorithm that assumes that illumination is sinusoidal and matches the nondistorted periodic pattern in the center of the sample [33]. We observe that the converging rays of the radial sample are misplaced. The artefacts are particularly visible far from the center where the pattern distortion is the most important. The first column of 6 images below the (a,b,c) figures corresponds to 6 of the 12 simulated measurements; the second column shows the actual illumination patterns that were used to create the simulated measurements; the third column shows the reconstructed illumination patterns using blind-SIM.





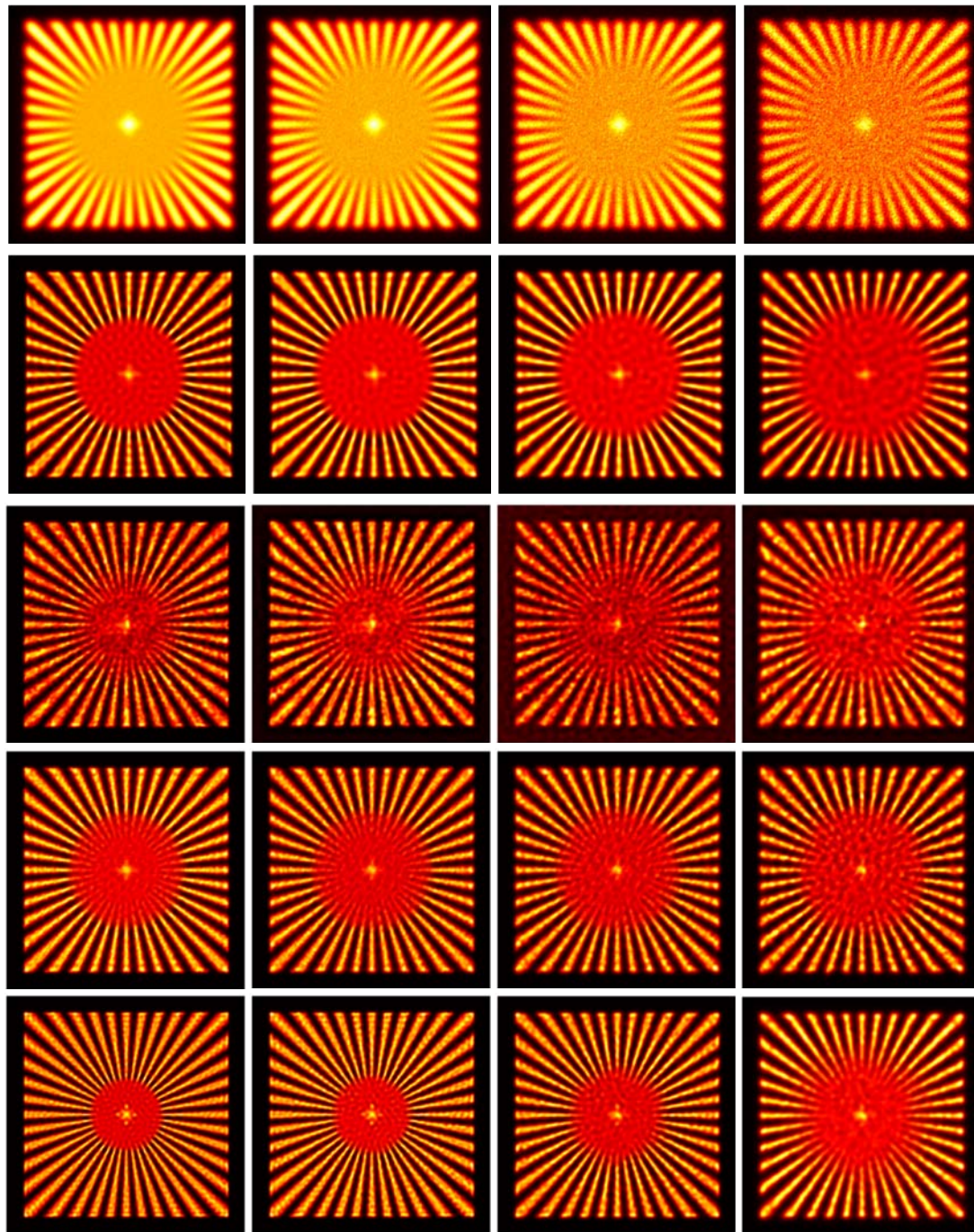


Fig. S4. **Reconstructed fluorescence density of the 'star-like' sample using different imaging techniques for various levels of photon noise.** The first row corresponds to the reconstructions obtained with Wide-Field, the second row corresponds to the Deconvolution, the third row to Speckle blind-SIM using 80 speckle images, the fourth row to Periodic Blind-SIM using 9 periodic SIM images and the fifth row to periodic SIM (with known illumination patterns) using the same 9 periodic SIM images. The first, second and third columns correspond to data corrupted with 6 electrons read-noise per Nyquist pixel and per measurement and simulated with a total average number of photons per Nyquist pixel of 40,000, 10,000 and 2,500 respectively. The fourth column corresponds to data corrupted with 1 electron read-noise per Nyquist pixel and per measurement and simulated with a total average number of 600 photons per Nyquist pixel. See section 2.B for more details on the simulation and Table S1 for a quantitative estimation of the resolution of the 20 reconstructions. Whatever the level of noise, blind-SIM is always better than Deconvolution and its resolution is close to that of periodic SIM though with less contrasted periodic patterns. The granular aspect of Speckle blind-SIM is due to the residual inhomogeneity of the average illumination which is performed over 80 speckles only. The side of each square image is  $10\lambda$ .



## References

- [21] Bouman, C. and Sauer, K. A unified approach to statistical tomography using coordinate descent optimization. *IEEE Transaction on image processing* **5**(3), 480–492, MAR (1996).
- [22] Allain, M. and Roques, J.-P. Imaging techniques for gamma-ray diffuse emission: application to integral/spi. *A&A* **447**(3), 1175–1187 (2006).
- [23] Press, W. H., Flannery, B. P., Teukolski, S. A., and Vetterling, W. T. *Numerical recipes. The art of scientific computing*. Cambridge University Press, (1986).
- [24] Polak, E. and Ribière, G. Note sur la convergence de méthodes de directions conjuguées. *Rev. Francaise Informat. Recherche Opérationnelle* **3**(16), 35–43 (1969).
- [25] Bertero, M. and Boccacci, P. A simple method for the reduction of boundary effects in the richardson-lucy approach to image deconvolution. *A&A* **437**(1), 369–374 (2005).
- [26] Vio, R., Bardsley, J., Donatelli, M., and Wamsteker, W. Dealing with edge effects in least-squares image deconvolution problems. *A&A* **442**(1), 397–403 (2005).
- [27] Pawley, J. B. Points, pixels, and gray levels: Digitizing image data. In *Handbook Of Biological Confocal Microscopy*, Pawley, J. B., editor, 59–79. Springer US (2006).
- [28] Pham, T. Q., Bezuijen, M., van Vliet, L. J., Schutte, K., and Hendriks, C. L. L. Performance of optimal registration estimators. *Proc. SPIE* **5817**, 133 (2005).
- [29] Sementilli, P. J., Hunt, B. R., and Nadar, M. S. Analysis of the limit to superresolution in incoherent imaging. *J. Opt. Soc. Am. A* **10**(11), 2265–2276, Nov (1993).
- [30] Hansen, P. *Rank-deficient and Discrete Ill-posed Problems: Numerical Aspects of Linear Inversion*. SIAM, Philadelphia, (1998).
- [31] Golub, G. H., Heath, M., and Wahba, G. Generalized cross-validation as a method for choosing a good ridge parameter. *Technometrics* **21**(2), 215–223, May (1979).
- [32] Bertero, M. and Boccacci, P. *Introduction to inverse problems in imaging*. Institute of Physics Pub., London, (1998).
- [33] Sentenac, A., Belkebir, K., Giovannini, H., and Chaumet, P. C. High-resolution total-internal-reflection fluorescence microscopy using periodically nanostructured glass slides. *J. Opt. Soc. Am. A* **26**(12), 2550–2557, Dec (2009).
- [34] Stelzer, E. Contrast, resolution, pixelation, dynamic range and signal-to-noise ratio: fundamental limits to resolution in fluorescence light microscopy. *Journal of Microscopy - Oxford* **189**(Part 1), 15–24, Jan (1998).